

Construction of a Scanning Ion-Conductance Microscope for Tip-Enhanced Raman Spectroscopy

Xing He, Leonardo Scarabelli, and Naihao Chiang*



Cite This: <https://doi.org/10.1021/acs.analchem.5c02986>



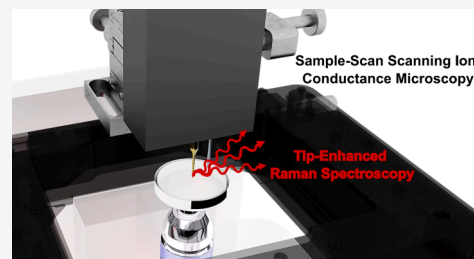
Read Online

ACCESS |

Metrics & More

Article Recommendations

ABSTRACT: Tip-enhanced Raman spectroscopy (TERS) has been developed by using atomic force microscopy and scanning tunneling microscopy since its birth in the early 2000s. Because, in principle, any scanning probe microscopy (SPM) can be combined with TERS, there is an increasing interest in extending TERS to other SPMs, especially the liquid-phase ones, targeting applications in biological or catalytic systems. We present the design, construction, and characterization of a laser-coupled scanning ion-conductance microscope (SICM) integrated with TERS for near-field spectroscopy under liquid environments. Key design elements include a full sample-scanning SICM, optics for TERS, and noise-isolating methods. The SICM-TERS system demonstrates direct-current and alternating-current SICM imaging modes on polydimethylsiloxane (PDMS) structures. Furthermore, the TERS capability was tested using silica-nanosphere-grafted PDMS. This work illustrates the feasibility and performance of SICM-TERS as a versatile tool for label-free nanoscale spectroscopy, opening new possibilities for real-time, *in situ* analysis of soft matter, electrochemical, and biological systems.



INTRODUCTION

Tip-enhanced Raman spectroscopy (TERS) is an emerging label-free chemical imaging technique suitable for investigating fundamental surface and interfacial phenomena.¹ It combines the structural sensitivity of surface-enhanced Raman spectroscopy (SERS) with the nanoscale spatial resolution of scanning probe microscopy (SPM) to achieve the ultimate spatial resolution in optical spectroscopy: Ångström-scale resolution.² Initially, TERS instrumentation involved ambient atomic force microscopy (AFM) and subsequently extended to the ultrahigh vacuum scanning tunneling microscopes (UHV-STM),³ providing unprecedented spatial resolution in Raman spectroscopic imaging.^{4–9} By overcoming the optical diffraction limits, deeper insight into phenomena otherwise unattainable due to limited spatial resolution was revealed, including the subensemble behavior of adsorbates on surfaces,^{10–12} local electric field distribution,^{13,14} and single-molecule chemistry.^{15,16} Recently, TERS under liquid environments has also been demonstrated with liquid-phase AFM^{17–19} and electrochemical STM.^{20–23}

Even though STM and AFM are the most popular types of SPM, many more SPMs have been designed and built to provide imaging contrast based on other nanoscale confined phenomena, including scanning electrochemical microscopy (SECM),^{24–28} scanning ion-conductance microscopy (SICM),^{29–32} and scanning nitrogen-vacancy center magnetometry (SNVM),^{33,34} to name a few examples. In principle, TERS could be readily implementable in all types of SPM, assuming that the nanoscale probes can be fabricated with plasmonic materials. For instance, STM-TERS uses electro-

chemically etched Au or Ag tips,^{35,36} and AFM-TERS uses Au- or Ag-coated cantilevers.^{37,38} Additionally, other considerations, such as the stability of the SPMs and integration of optics, need to be taken into account for the integration of TERS with SPMs.

Herein, we report on the design and performance of a laser-coupled SICM apparatus capable of nanoscale imaging and TERS under liquid environments. The entire SICM setup is mounted onto an inverted optical microscope, which is commonly employed in imaging applications, facilitating the simple exchange of the nanopipette, providing at the same time a low electronic noise. Additionally, this SICM setup can be readily interfaced with commercial SPM controllers and achieve direct-current (DC), alternating current (AC) SICM imaging, and TERS with a gold-coated quartz nanopipette. This custom-built SICM-TERS instrument is expected to characterize materials' performances toward nanoscale Raman imaging at solid–liquid interfaces (*in vitro* and *in situ* electrochemical environments).

Received: May 18, 2025

Revised: July 13, 2025

Accepted: July 21, 2025

DESIGN CONSIDERATIONS

The main design considerations for SICM-TERS instrumentation are those that directly influence the stability of the SICM probe–sample interaction and the Raman signal collection efficiency. On the SICM side, these include the structural stability of the system, vibrational and electronic noise isolation, and the quality of the SPM controller. Integrating the near-field Raman spectroscopic measurement introduces additional levels of complexity for maintaining the laser focus on the probe tip. Figure 1 provides a general overview of the complete SICM-TERS system and the corresponding instrumentation described herein.

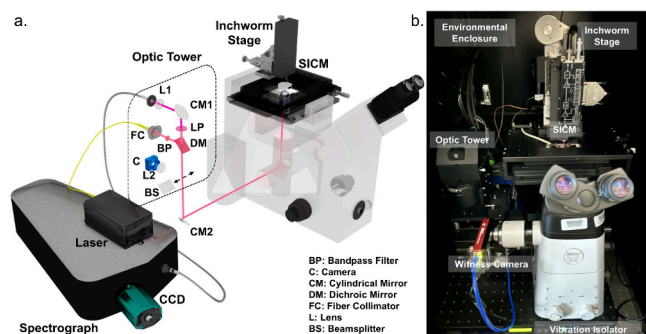


Figure 1. Overview of SICM-TERS instrument. (a) Schematics and (b) photograph of the complete setup. The SICM setup is housed on an inverted microscope and placed inside a custom-built environmental enclosure. A compact optical tower is used to fiber-couple the laser excitation and signal detection from outside the enclosure.

Optics for TERS Integration. Performing Raman spectroscopy through commercial microscopes is one of the most reliable ways to introduce laser excitation and take advantage of efficient signal collection through high numerical aperture (NA) microscope objectives. Inspired by previous ambient TERS optics, the SICM-TERS setup (Figure 1) uses an inverted microscope (Eclipse Ti2, Nikon) as the base and a fiber-optics-based optical tower to couple the laser excitation and Raman signals in and out of an environmental enclosure. A commercial Raman optic tower (Alpha300, WITec) that contains all of the necessary optical elements was used for our setup. In short, the laser excitation enters the optical tower through a fiber collimator, followed by a laser cleanup bandpass filter to remove the glass Raman signals originating from the fiber optics. A dichroic mirror is used to divert the cleaned-up laser excitation to exit the optical tower, enter a side port of the inverted microscope, and focus on the sample through a microscope objective (NA 0.6, Plan Fluor 40X, Nikon). The same objective collects the backscattered Raman signal and follows the same optical path back to the optical tower. The Rayleigh scattering is removed by a long-pass filter before focusing the spectroscopic signal into the collection fiber. Using an inverted microscope allows for the easy integration of SICM on top of the microscope. At the same time, the compact fiber-coupled optical tower enables the placement of a laser and spectrometer outside the environmental enclosure to cut down the overall noise level.

To achieve TERS, the laser must be aligned at the tip apex. An inchworm-motor-controlled 3-axis stage (TSE-820, Burleigh Instruments) with 20 nm encoder resolution was used to place and maintain the SICM nanopipette's position at the laser focus on top of the sample stage. The alignment

procedure started with moving the nanopipette into the laser focus by imaging through a witness camera via an insertable brightfield beamsplitter (Figure 2a). Depending on the witness

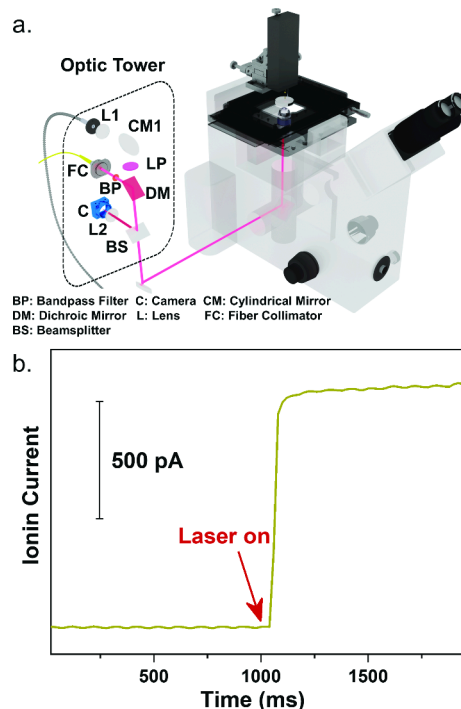


Figure 2. SICM-TERS nanopipette alignment. (a) Schematic showing the brightfield beamsplitter inserted, guiding the laser to the witness camera. (b) The ionic current response to a 10 mW 785 nm laser focused at the plasmonic nanopipette apex.

camera sensitivity and the maximum laser output power, the beamsplitter could be potentially replaced with 0/90 or 30/70 (reflection/transmission) beamsplitters. Furthermore, the ionic current changes when the optimal laser alignment is achieved (Figure 2b). Even though similar phenomena were observed for UHV-STM-TERS,³⁹ the detailed mechanism might be different as the change in the detected ionic current could be attributed to the higher convection at the nanopipette apex, which is caused by the mesoscopic plasmonic heating effect.⁴⁰ Finally, monitoring the ionic current response during alignment not only provides finer control over nanopipette position but also allows the stability of the ionic current to serve as an indicator for nanoscale bubble formations, as bubbles may temporarily block ion flow.⁴¹

Noise Isolation. Like all other SPM techniques, a nanoscale SICM spatial resolution is achieved by measuring and maintaining nanoscale changes in distance-dependent physical quantities through a PID feedback loop: ionic current on the order of nanoamperes. Raman scattering is a weak optical process and can be easily buried under ambient light. Therefore, isolating vibrational, acoustic, and ambient light noise is essential for successful SICM-TERS measurement. A triple-function environmental enclosure shields the system from the disturbances mentioned above (not shown). An 18-unit (18U) steel server rack is repurposed to be the main body of the enclosure, acting as a Faraday cage. Acoustic isolation is achieved by continuously lining the enclosure exterior with a commercially available sound-deadening mat composed of layered butyl mastic, polyethylene (PE) foam, and a mass-

loaded butyl membrane. Foam insulation tapes were used to seal the edges of the enclosure. When the padded enclosure is fully closed, the overall sound level at the sample position decreases from ~65 to 42 dB.

The combination of the two methods achieves low-frequency vibration isolation of our SICM setup. First, the enclosure is mounted on a floating stainless steel optical table (S-2000, Newport), with the added benefit of the server rack being electrically connected to a large metallic table that serves as a common ground point. Second, the inverted microscope housing the SICM is placed on a benchtop active vibration isolator (TS-150, Herzan) to filter low-frequency vibrations further. Figure 3 summarizes the effects of each vibration

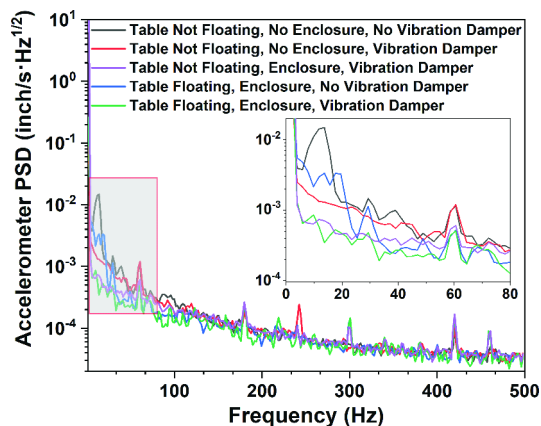


Figure 3. Comparison of the noise isolation with the custom-built environmental enclosure, a floating optical table, and an active vibration damper measured by an accelerometer. The zoomed inset shows the instrumental vibration responses from 0 to 80 Hz.

isolation method characterized by an accelerometer. Overall, the active vibration damper in combination with the environmental enclosure was the most effective in reducing low-frequency vibrations (<20 Hz) that affected the tip-sample junction stability the most. The floating of the laser table improved the isolation above 20 Hz, but the effect was moderate. Considering the challenge of liquid-phase operation, having the environmental enclosure, a floating laser table, and an additional active vibration damper provides the most stable SICM imaging condition.

Sample-Scan SICM. Typically, most SICM decouples the vertical (Z) piezoelectric scanner from the lateral (X/Y) one for better imaging stability, as in practical applications of SICM to soft materials and biological systems the vertical movement of the tips can be on the order of micrometers. However, such movement is greater than the focal depth of high numerical aperture (NA) objectives for obtaining high signal-to-noise ratio Raman spectra, posing a challenge to maintain the laser focused on the tip apex during TERS imaging experiments. Therefore, we opted for sample scanning in all three dimensions (X, Y, and Z), addressing this technical issue using a low-profile piezo flexure scanning stage (P-545, Physik Instrumente) to achieve the required nanoscale resolution. Additionally, a manual coarse positioning stage (M-545, Physik Instrumente) was installed underneath the 3D-scanner and a stage-top heater (QS-Heat35, AutoMate Scientific) on the scanner for temperature control in future *in vitro* biological experiments.

In a typical SICM experiment, ionic current (i_i) is on the order of nanoamperes (nA) or lower. For detecting such a small current, the background electronic noise was minimized by directly connecting the electrode inside the nanopipette to the current preamp with the shortest conductor. A customized aluminum adaptor plate (Figure 4) was machined to secure a

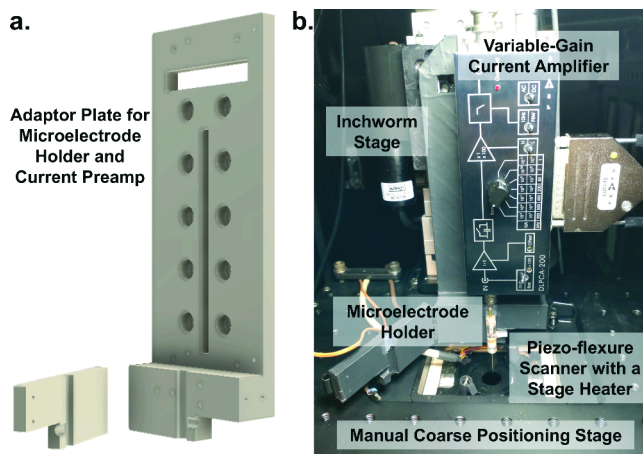


Figure 4. 3D design (a) and photograph (b) of the adaptor plate connect a variable-gain current preamp, microelectrode holder, and the inchworm motorized three-axis micrometer stage.

variable-gain current preamp (DLPCA-200, FEMTO) and contains a hollowed-out compartment to house commercial microelectrode holders (MEH2SW, World Precision Instruments). The aluminum compartment was joined with hinges and spring-loaded latches for mini-jewelry boxes, with the added benefit that it acted as an additional Faraday cage shielding the microelectrode holder. The finished adapter plate was covered with matte black anodized aluminum tape to reduce reflection and scattering from the lasers when performing SICM-TERS.

SICM IMAGING AND TERS PERFORMANCE

Compared to AFM, nanoscale SICM imaging causes less sample deformation,⁴² making it an ideal SPM technique for big but soft samples such as soft polymers and cell cultures. Polydimethylsiloxane (PDMS) protrusions, following a previously reported fabrication procedure,⁴³ were used to mimic the potential systems of interest of SICM-TERS. Both the direct-current (DC) and bias-modulated alternating-current (AC) SICM⁴⁴ modes were tested with an ~200 nm opening quartz nanopipette (Figure 5). Both feedback modes showed the signature drop of the DC- and AC-modulated ionic current as the nanopipette approached the PDMS surface.

To demonstrate the effectiveness of the implemented noise isolation measuring system, a square spiral was imaged with both SICM modes (Figure 5b, d). Even small defects, such as the thinning and tapering of the long edge and small deformation in the center, were clearly visible in a 1.5 mL 0.1 mM KCl bath in a 35 mm polymer-based Petri dish (μ -Dish, ibidi). The AC-SICM image (Figure 5d) showed a better vertical resolution since the nanopipette was closer to the sample. As a result, the small step along the PDMS edges from the lithographic process of the mold was well resolved. Overall, sample scanning in all three spatial dimensions did not seem to affect the imaging quality and stability of the custom-built SICM.

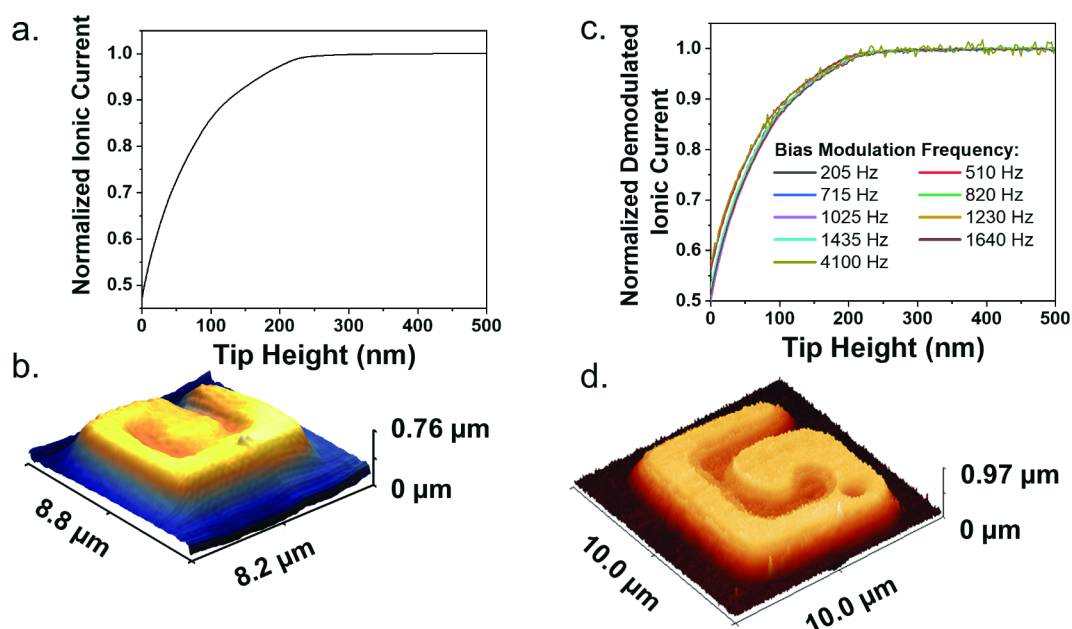


Figure 5. Direct-current (DC) SICM approaching curve (a) and topographic image (b) of a PDMS square spiral protrusion and bias-modulated alternating-current SICM approaching curve (c) and topographic image (d). DC-SICM conditions: $V_b = 0.3$ V, $i_i = 3.8$ nA. AC-SICM conditions: $V_b = -0.3$ V, $i_i^{AC} = 1.2$ nA, $\Delta V = 0.2$ V @ 312 Hz.

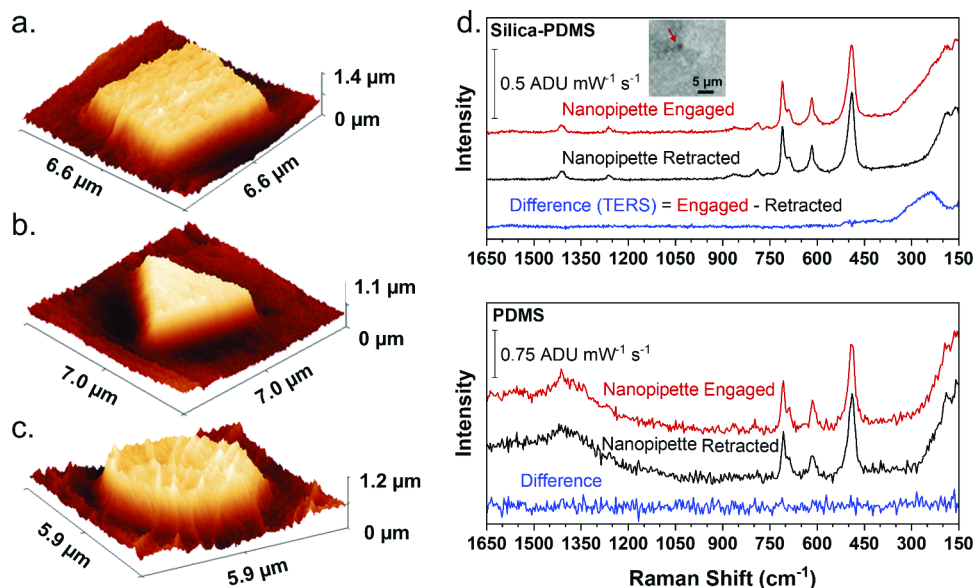


Figure 6. Three-dimensional representation of the DC-SICM image of a 5 μm (a) square, (b) triangle, and (c) circle from the PDMS stamp. (d) SICM-TERS of the silica-nanosphere-decorated PDMS with a 785 nm near-IR laser excitation. DC-SICM conditions: $V_b = 0.6$ V, $i_i = 14.65$ nA. SICM-TERS conditions: 20 mW, 60 s acquisition with 5 accumulations. Inset: optical micrograph of the triangular protrusion where the TERS spectra were acquired. The nanopipette (red arrow) was moved to the side to see the triangle. The plasmonic probe engaged and retracted spectra on clean PDMS show no difference under 5 mW laser excitation and 5 s acquisition with 10 accumulations.

To achieve SICM-TERS, the quartz nanopipette was one-sided sputter-coated with gold as described previously.⁴⁵ To create topographical and spectral contrast, silica nanospheres (177 nm, Bangs Laboratories) were grafted onto square, triangular, and circular PDMS protrusions (Figure 6a–c) by activating the PDMS with air plasma. The 3D inchworm motors were used to precisely place the plasmonic nanopipette at the laser focus with the aid of a witness camera on the optical tower. Figure 6d shows a SICM-TERS spectrum of silica-decorated PDMS with 785 nm excitation. The retracted spectrum was taken after the engaged spectrum with the probe

retracted ~ 500 nm from the sample. (The retracted distance was larger than the SICM sensing regime but within the laser focal spot, ensuring the difference in signal intensity was from the plasmonic nanopipette in the proximity of the sample surface.) The strong enhancement from the tip was sufficient for observing the silica nanoparticles, but no enhanced PDMS fingerprint modes were observed. The absence of SICM-TERS of PDMS can be attributed to the low Raman cross-section of PDMS and/or the subnanometer working distance of SICM-TERS⁴⁵ smaller than the diameter of the silica nanosphere. Consequently, the plasmonic nanopipette engaged and

retracted spectra taken on a clean PDMS showed no difference. Furthermore, the silica Raman modes alter significantly depending on the manufacturing conditions, thickness, and impurities;^{46–48} in combination with the small probe volume of SICM-TERS, the enhanced Raman spectrum appears to be different than the one from bulk fused silica. Nonetheless, the constructed instrument was capable of achieving SICM-TERS, paving the way for nanoscale chemical imaging of soft interfaces in liquid environments.

CONCLUSION

In summary, we have presented the design and construction of a laser-coupled sample-scanning SICM capable of TERS under an electrolytic environment. Key design considerations and the subsequent proof-of-concept performance of SICM-TERS have been presented. The sample-scan design approach has maintained the laser focus at the probe apex for TERS without sacrificing the SICM imaging capability with all necessary noise isolation measures in place. Future improvements in Raman detection efficiency, such as using an ultra-deep depletion CCD or an amplified photodiode detector connected to a lock-in amplifier, could enable the detection of weak Raman scattering analytes and benefit the TERS imaging speed. This SICM-TERS system thereby provides a solid foundation for future high-performance method development toward *in situ* nanoscale chemical imaging of soft and biological material interfaces.

AUTHOR INFORMATION

Corresponding Author

Naihao Chiang – Department of Chemistry, University of Houston, Houston, Texas 77204, United States;
✉ orcid.org/0000-0003-3782-6546; Email: nchiang@uh.edu

Authors

Xing He – Department of Chemistry, University of Houston, Houston, Texas 77204, United States

Leonardo Scarabelli – NanoOddLAB, Department of Chemistry and Process & Resource Engineering, University of Cantabria, Santander 39005, Spain; ✉ orcid.org/0000-0002-6830-5893

Complete contact information is available at:

<https://pubs.acs.org/10.1021/acs.analchem.5c02986>

Notes

The authors declare no competing financial interest.

ACKNOWLEDGMENTS

X.H. and N.C. acknowledge support from the National Institute of Biomedical Imaging and Bioengineering (NIBIB Grant R00EB028325). N.C. acknowledges support from the National Science Foundation (CHE-2304955). L.S. acknowledges support from the Spanish Ministerio de Ciencia e Innovación through fellowship RYC2022-037894-I.

REFERENCES

- (1) Bao, Y.-F.; Zhu, M.-Y.; Zhao, X.-J.; Chen, H.-X.; Wang, X.; Ren, B. *Chem. Soc. Rev.* **2024**, 53 (20), 10044–10079.
- (2) Zrimsek, A. B.; Chiang, N.; Mattei, M.; Zaleski, S.; McAnally, M. O.; Chapman, C. T.; Henry, A.-I.; Schatz, G. C.; Van Duyne, R. P. *Chem. Rev.* **2017**, 117 (11), 7583–7613.
- (3) Pozzi, E. A.; Goubert, G.; Chiang, N.; Jiang, N.; Chapman, C. T.; McAnally, M. O.; Henry, A.-I.; Seideman, T.; Schatz, G. C.; Hersam, M. C.; Duyne, R. P. V. *Chem. Rev.* **2017**, 117 (7), 4961–4982.
- (4) Chiang, N.; Chen, X.; Goubert, G.; Chulhai, D. V.; Chen, X.; Pozzi, E. A.; Jiang, N.; Hersam, M. C.; Seideman, T.; Jensen, L.; Van Duyne, R. P. *Nano Lett.* **2016**, 16 (12), 7774–7778.
- (5) Xu, J.; Zhu, X.; Tan, S.; Zhang, Y.; Li, B.; Tian, Y.; Shan, H.; Cui, X.; Zhao, A.; Dong, Z.; Yang, J.; Luo, Y.; Wang, B.; Hou, J. G. *Science* (1979) **2021**, 371 (6531), 818–822.
- (6) Mahapatra, S.; Li, L.; Schultz, J. F.; Jiang, N. *J. Chem. Phys.* **2020**, 153 (1), 010902.
- (7) Li, L.; Schultz, J. F.; Mahapatra, S.; Liu, X.; Shaw, C.; Zhang, X.; Hersam, M. C.; Jiang, N. *J. Am. Chem. Soc.* **2021**, 143 (38), 15624–15634.
- (8) Wang, R.-P.; Hu, C.-R.; Han, Y.; Yang, B.; Chen, G.; Zhang, Y.; Zhang, Y.; Dong, Z.-C. *J. Phys. Chem. C* **2022**, 126 (29), 12121–12128.
- (9) Lee, J.; Crampton, K. T.; Tallarida, N.; Apkarian, V. A. *Nature* **2019**, 568, 78–82.
- (10) Chiang, N.; Jiang, N.; Madison, L. R.; Pozzi, E. A.; Wasielewski, M. R.; Ratner, M. A.; Hersam, M. C.; Seideman, T.; Schatz, G. C.; Van Duyne, R. P. *J. Am. Chem. Soc.* **2017**, 139 (51), 18664–18669.
- (11) Li, L.; Mahapatra, S.; Schultz, J. F.; Zhang, X.; Jiang, N. *ACS Nano* **2024**, 18 (46), 32118–32125.
- (12) Li, L.; Mahapatra, S.; Schultz, J. F.; Zhang, X.; Jiang, N. *Chem.* **2025**, 11 (1), 102290–102299.
- (13) Wang, C.-F.; Krayev, A. V.; El-Khoury, P. Z. *Nano Lett.* **2023**, 23 (19), 9114–9118.
- (14) El-Khoury, P. Z. *Chem. Commun.* **2023**, 59 (24), 3536–3541.
- (15) Mahapatra, S.; Schultz, J. F.; Li, L.; Zhang, X.; Jiang, N. *J. Am. Chem. Soc.* **2022**, 144 (5), 2051–2055.
- (16) Kazuma, E.; Lee, M.; Jung, J.; Trenary, M.; Kim, Y. *J. Phys. Chem. C* **2023**, 127 (23), 10953–10959.
- (17) Mrdenović, D.; Ge, W.; Kumar, N.; Zenobi, R. *Angew. Chem., Int. Ed.* **2022**, 61 (43), No. e202210288.
- (18) Mrdenović, D.; Tang, Z.-X.; Pandey, Y.; Su, W.; Zhang, Y.; Kumar, N.; Zenobi, R. *Nano Lett.* **2023**, 23 (9), 3939–3946.
- (19) Kang, G.; Yang, M.; Mattei, M. S.; Schatz, G. C.; Van Duyne, R. P. *Nano Lett.* **2019**, 19 (3), 2106–2113.
- (20) Martín Sabanés, N.; Ohto, T.; Andrienko, D.; Nagata, Y.; Domke, K. F. *Angew. Chem., Int. Ed.* **2017**, 56 (33), 9796–9801.
- (21) Goubert, G.; Chen, X.; Jiang, S.; Van Duyne, R. P. *J. Phys. Chem. Lett.* **2018**, 9 (14), 3825–3828.
- (22) Fiocco, A.; Pavlic, A. A.; Kanoufi, F.; Maisonhaute, E.; Noël, J.-M.; Lucas, I. T. *Anal. Chem.* **2024**, 96 (7), 2791–2798.
- (23) Huang, S.-C.; Zhao, Q.-Q.; Feng, H.-S.; Ma, H.; Zhao, L.; Wang, X.; Ren, B. *J. Phys. Chem. C* **2023**, 127 (26), 12568–12575.
- (24) Mishra, A.; Zorigt, M.; Kim, D. O.; Rodríguez-López, J. J. *Am. Chem. Soc.* **2024**, 146 (13), 8847–8851.
- (25) Ashaduzzaman, M.; Pan, S. J. *Phys. Chem. Lett.* **2025**, 16 (3), 818–825.
- (26) Putnam, S. T.; Santiago-Carboney, A.; Qian, P.; Rodríguez-López, J. *Anal. Chem.* **2025**, 97 (15), 8147–8181.
- (27) Gao, R.; Edwards, M. A.; Qiu, Y.; Barman, K.; White, H. S. *J. Am. Chem. Soc.* **2020**, 142 (19), 8890–8896.
- (28) Bo, T.; Ghoshal, D.; Wilder, L. M.; Miller, E. M.; Mirkin, M. V. *ACS Nano* **2025**, 19 (3), 3490–3499.
- (29) Wang, Y.; Shashishekar, M.; Spence, D. M.; Baker, L. A. *ACS Measurement Science Au* **2025**, 5 (3), 345–352.
- (30) Zhu, C.; Huang, K.; Siepsner, N. P.; Baker, L. A. *Chem. Rev.* **2021**, 121 (19), 11726–11768.
- (31) Hagemann, P.; Gesper, A.; Happel, P. *ACS Nano* **2018**, 12 (6), 5807–5815.
- (32) Leitao, S. M.; Drake, B.; Pinjusic, K.; Pierrat, X.; Navikas, V.; Nievergelt, A. P.; Brillard, C.; Djekic, D.; Radenovic, A.; Persat, A.; Constam, D. B.; Anders, J.; Fantner, G. E. *ACS Nano* **2021**, 15 (11), 17613–17622.

- (33) Žaper, L.; Rickhaus, P.; Wyss, M.; Gross, B.; Wagner, K.; Poggio, M.; Braakman, F. *ACS Appl. Nano Mater.* **2024**, *7* (4), 3854–3860.
- (34) Qiu, Z.; Hamo, A.; Vool, U.; Zhou, T. X.; Yacoby, A. *npj Quantum Inf* **2022**, *8* (1), 107.
- (35) Mahapatra, S.; Li, L.; Schultz, J. F.; Jiang, N. *J. Raman Spectrosc.* **2021**, *52* (2), 573–580.
- (36) Zhang, X.-B.; Zhang, Y.-F.; Li, H.; Cui, J.; Jiang, S.; Yang, B.; Zhang, Y.; Zhang, Y.; Dong, Z.-C. *Chinese Journal of Chemical Physics* **2022**, *35* (5), 713–719.
- (37) Bartolomeo, G. L.; Goubert, G.; Zenobi, R. *Appl. Spectrosc.* **2020**, *74* (11), 1358–1364.
- (38) Yang, L.-K.; Huang, T.-X.; Zeng, Z.-C.; Li, M.-H.; Wang, X.; Yang, F.-Z.; Ren, B. *Nanoscale* **2015**, *7* (43), 18225–18231.
- (39) Pal, P. P.; Jiang, N.; Sonntag, M. D.; Chiang, N.; Foley, E. T.; Hersam, M. C.; Van Duyne, R. P.; Seideman, T. *J. Phys. Chem. Lett.* **2015**, *6* (21), 4210–4218.
- (40) Vinnacombe-Willson, G. A.; Chiang, N.; Scarabelli, L.; Hu, Y.; Heidenreich, L. K.; Li, X.; Gong, Y.; Inouye, D. T.; Fisher, T. S.; Weiss, P. S.; Jonas, S. J. *ACS Cent Sci.* **2020**, *6* (11), 2105–2116.
- (41) Hu, Y.-X.; Ying, Y.-L.; Gao, R.; Yu, R.-J.; Long, Y.-T. *Anal. Chem.* **2018**, *90* (21), 12352–12355.
- (42) Seifert, J.; Rheinlaender, J.; Novak, P.; Korchev, Y. E.; Schaffer, T. E. *Langmuir* **2015**, *31* (24), 6807–6813.
- (43) Chiang, N.; Scarabelli, L.; Vinnacombe-Willson, G. A.; Pérez, L. A.; Dore, C.; Mihi, A.; Jonas, S. J.; Weiss, P. S. *ACS Mater. Lett.* **2021**, *3* (3), 282–289.
- (44) McKelvey, K.; Perry, D.; Byers, J. C.; Colburn, A. W.; Unwin, P. R. *Anal. Chem.* **2014**, *86* (7), 3639–3646.
- (45) He, X.; Tareq, A. M.; Qi, K.; Conti, Y.; Tung, V.; Chiang, N. *Nano Lett.* **2024**, *24* (43), 13805–13810.
- (46) Mélinon, P.; Kéghélian, P.; Prével, B.; Dupuis, V.; Perez, A.; Champagnon, B.; Guyot, Y.; Pellarin, M.; Lermé, J.; Broyer, M.; Rousset, J. L.; Delichère, P. *J. Chem. Phys.* **1998**, *108* (11), 4607–4613.
- (47) Neuville, D. R.; Charpentier, T.; Du, J. C.; Yue, Y. Z.; Blanc, W.; Cicconi, M. R.; Lancry, M.; Ren, M. Structure Characterizations and Molecular Dynamics Simulations of Melt, Glass, and Glass Fibers. In *Fiberglass Science and Technology: Chemistry, Characterization, Processing, Modeling, Application, and Sustainability*; Li, H., Ed.; Springer International Publishing: Cham, 2021; pp 89–216.
- (48) Liu, H.; Kaya, H.; Lin, Y.-T.; Ogrinc, A.; Kim, S. H. *J. Am. Ceram. Soc.* **2022**, *105* (4), 2355–2384.